



Direct Numerical Simulation of Nozzle-Wall Pressure Fluctuations in a Mach 8 Wind Tunnel

Lian Duan*, Gary L. Nicholson†, and Junji Huang‡
 Missouri University of Science and Technology, Rolla, MO 65409, USA

Katya M. Casper§, Ross M. Wagnild¶, and Neal P. Bitter||
 Sandia National Laboratories, Albuquerque, NM 87185, USA

Direct numerical simulations (DNS) of the full-scale axisymmetric nozzle of a Mach 8 wind tunnel are conducted with an emphasis on characterizing the properties of the pressure fluctuations induced by the turbulent boundary layer (TBL) along the nozzle wall. The axisymmetric nozzle geometry and the flow conditions of the DNS match those of the Sandia Hypersonic Wind Tunnel at Mach 8. The mean and turbulence statistics of the nozzle-wall boundary layer show good agreement with those predicted by Pate's correlation and Reynolds Averaged Navier-Stokes (RANS) computations. The wall-pressure intensity, power spectral density, and coherence predicted by DNS show good comparisons with those measured in the same tunnel. The Corcos model is found to deliver good prediction of wall pressure coherence over intermediate and high frequencies. The streamwise and spanwise decay constants at Mach 8 are similar to those predicted by DNS and experiments at lower supersonic Mach numbers.

Nomenclature

C_p	=	heat capacity at constant pressure, J/(K·kg)
C_v	=	heat capacity at constant volume, J/(K·kg)
H	=	shape factor, $H = \delta^*/\theta$, dimensionless
M	=	Mach number, dimensionless
P_o	=	total pressure, Pa
Pr	=	Prandtl number, $Pr = 0.71$, dimensionless
R	=	ideal gas constant, $R = 287$, J/(K·kg), or radius of the axisymmetric nozzle, m
Re_θ	=	Reynolds number based on momentum thickness and freestream viscosity, $Re_\theta \equiv \frac{\rho_\infty U_\infty \theta}{\mu_\infty}$, dimensionless
Re_{δ_2}	=	Reynolds number based on momentum thickness and wall viscosity, $Re_{\delta_2} \equiv \frac{\rho_\infty U_\infty \theta}{\mu_w}$, dimensionless
Re_τ	=	Reynolds number based on shear velocity and wall viscosity, $Re_\tau \equiv \frac{\rho_w u_\tau \delta}{\mu_w}$, dimensionless
rms	=	root mean square
T	=	temperature, K
T_o	=	total temperature, K
T_r	=	recovery temperature, $T_r = T_\infty(1 + 0.9 * \frac{\gamma-1}{2} M_\infty^2)$, K
U_∞	=	freestream velocity, m/s
a	=	speed of sound, m/s
p	=	pressure, Pa
q	=	dynamic pressure, Pa
r	=	radial coordinate
u	=	streamwise velocity, m/s
u_τ	=	friction velocity, m/s

*Assistant Professor, Senior Member, AIAA

†Graduate Student, Department of Mechanical and Aerospace Engineering, Student Member, AIAA

‡Graduate Student, Department of Mechanical and Aerospace Engineering, Student Member, AIAA

§Principal Member of the Technical Staff. Senior Member AIAA.

¶Principal Member of the Technical Staff. Senior Member AIAA.

||Principal Member of the Technical Staff. Senior Member AIAA.

v	=	spanwise velocity, m/s
w	=	wall-normal velocity, m/s
x	=	streamwise direction of the right hand Cartesian coordinate
y	=	spanwise direction of the right hand Cartesian coordinate
z	=	wall-normal direction of the right hand Cartesian coordinate
z_τ	=	viscous length, $z_\tau = \nu_w/u_\tau$, m
γ	=	specific heat ratio, $\gamma = C_p/C_v$, dimensionless
δ	=	boundary layer thickness, m
δ^*	=	displacement thickness, m
κ	=	thermal conductivity, $\kappa = \mu C_p/Pr$, W/(m·K)
θ	=	momentum thickness, m
μ	=	dynamic viscosity, $\mu = 1.458 \times 10^{-6} \frac{T^{3/2}}{T+110.4}$, kg/(m·s)
ν	=	kinematic viscosity, $\nu = \mu/\rho$, m ² ·s
ρ	=	density, kg/m ³
	=	
<i>Subscripts</i>	=	
i	=	inflow station for the domain of direct numerical simulations
o	=	stagnation quantities
rms	=	root mean square
w	=	wall variables
∞	=	freestream variables
	=	
<i>Superscripts</i>	=	
$+$	=	inner wall units
$\overline{(\cdot)}$	=	averaged variables
$(\cdot)'$	=	perturbation from averaged variable

I. Introduction

One of the primary sources of vibratory loading during atmospheric reentry is the wall-pressure fluctuations induced by hypersonic transitional and turbulent boundary layers. These pressure fluctuations can be intense enough to cause severe vibration of internal components and lead to damaging effects such as flutter. Characterizing these fluctuating pressure on vehicle surfaces is thus of practical importance to the structural design of hypersonic vehicles. So far, there is a lack of physics-based models that can adequately predict the magnitude, frequency content, location, and spatial extent of boundary-layer-induced pressure fluctuations at hypersonic speeds. The lack of predictive capability leads to heavier vehicles and degraded flight performance.

To improve prediction of hypersonic pressure fluctuations, experiments were conducted on a 7° sharp cone at zero angle of attack under noisy flow in the Sandia National Laboratories Hypersonic Wind Tunnel (HWT) at Mach 5, 8, and 14 [1]. The measured pressure loading on the cone surface was compared to that on wind tunnel nozzle walls at similar Mach numbers for developing statistical pressure fluctuation models [2]. The comparison showed that the measured pressure auto spectral densities for hypersonic flow over a sharp 7° half-angle cone at freestream Mach numbers of 5.0 and 7.9 have much higher magnitude than wind tunnel wall data at similar Mach numbers. Considering a higher freestream noise environment for the cone runs, the large discrepancies between the wind tunnel wall and cone data may suggest that tunnel noise significantly impacts the measurements of hypersonic pressure fluctuations on a test article mounted within a noisy hypersonic tunnel. The influence of tunnel noise is hard to clarify, however, by conducting a similar experiment in a quiet tunnel, as the existing quiet facilities are limited by their size and Reynolds number, and such limitations prevent a naturally generated turbulent boundary layer developing over a cone model [3].

The current work aims to complement the aforementioned experiments by direct numerical simulations (DNS) that simulate a cone experiment in a noisy hypersonic wind tunnel. Specifically, the DNS will shed light on the experimentally observed discrepancies in turbulent pressure fluctuations on the tunnel wall and over a seven-degree half angle cone mounted within a noisy hypersonic wind tunnel. As an initial step toward that goal, this paper reports preliminary DNS results of the nozzle-wall turbulent boundary layer in the Sandia Hypersonic Wind Tunnel at Mach 8 (Sandia HWT-8) and its induced pressure fluctuations on the nozzle wall. The single- and multi-point statistics of wall-pressure fluctuations of the DNS are compared to experiments.

The paper is structured as follows. The flow conditions and numerical methods are outlined in Section II. Section III discusses wind-tunnel experiments and flat-plate simulations for DNS validation. Section IV presents DNS predictions of nozzle-wall turbulent boundary layer for Sandia HWT-8 and the comparison of the DNS with wall-pressure measurements in the same tunnel. A summary of the current work is given in Section V.

II. Flow Conditions and DNS Methodology

Targeted flow conditions within the test section are summarized in Table 1, which fall within the range of nozzle conditions of the Sandia HWT-8. The wall temperature is 298 K, corresponding to a wall-to-total temperature ratio of $T_w/T_o \approx 0.48$. DNS of hypersonic turbulent boundary layers are conducted in an axisymmetric nozzle configuration with the same convergent-divergent nozzle contour as that of Sandia HWT-8. In addition to the nozzle configuration, DNS of a turbulent boundary layer developing spatially over a single flat wall is also conducted for validation and comparison with the nozzle simulation. The DNS simulations with nozzle and flat plate configurations are referred to as Case “DNS-Nozzle” and “DNS-FlatPlate”, respectively.

Table 1 Nominal freestream conditions for the DNS of a Mach 8 turbulent boundary layer.

Cases	M_∞	P_o (kPa)	T_o (K)	Re_{unit} (1/m)	T_w (K)
DNS-Nozzle	7.91	4692	617	13.4×10^6	298
DNS-FlatPlate	7.87	3482	694	8.2×10^6	298

A. Governing Equations and Numerical Methods

To simulate the turbulent boundary layer on the inner surface of an axisymmetric nozzle as that of the Sandia HWT-8, the full three-dimensional compressible Navier-Stokes equations in conservation form are solved numerically in cylindrical coordinates. The working fluid is nitrogen and falls within the perfect gas regime. The usual constitutive relations for a Newtonian fluid are used: the viscous stress tensor is linearly related to the rate-of-strain tensor, and the heat flux vector is linearly related to the temperature gradient through Fourier’s law. The coefficient of viscosity μ is computed from Keyes law [4], and the coefficient of thermal conductivity κ is computed from $\kappa = \mu C_p / Pr$, with the molecular Prandtl number $Pr = 0.71$.

The inviscid fluxes of the governing equations are computed using a seventh-order weighted essentially non-oscillatory (WENO) scheme. Compared with the original finite-difference WENO introduced by Jiang and Shu [5], the present scheme is optimized by means of limiters [6, 7] to reduce the numerical dissipation; WENO adaptation is limited to the boundary-layer region for maintaining numerical stability while the optimal stencil of WENO is used outside the boundary layer for optimal resolution of the radiated acoustic field. The viscous fluxes are discretized using a fourth-order central difference scheme and time integration is performed using a third-order low-storage Runge-Kutta scheme [8].

The singularity at the polar axis manifested in the $1/r$ terms of the governing equations is handled by shifting the grid points in the radial direction by half the mesh spacing following the approach proposed by Mohseni and Colonius [9]. The use of less accurate one-sided finite differencing schemes for the purpose of evaluating radial derivatives close to the pole ($r = 0$) is eliminated by mapping the flow domain from $(0, R) \times (0, 2\pi)$ to $(-R, R) \times (0, \pi)$, where R is the radius of the computational domain, according to the approach of Mohseni and Colonius [9]. In addition to the approach by Mohseni and Colonius [9], the singularity at the polar axis is also handled by using a technique based on power series expansions [10] and by solving the governing flow equations with a collocated grid (i.e., a solution point exists at the polar axis ($r = 0$)). For the statistics reported in the paper, negligible differences are found between the two approaches. The time step limitation due to the decrease in azimuthal spacing in the vicinity of centerline (or pole) is addressed by dropping every few grid points (which amounts to increasing the grid spacing) in the azimuthal direction as $r \rightarrow 0$ in computation of the azimuthal derivative [11].

The details of the DNS methodology have been documented in our previous simulations of acoustic radiation by turbulent boundary layers [12–16].

B. Simulation Setup and Boundary Conditions

A precursor RANS simulation was first conducted using the ANSYS Fluent code [17] for initializing the DNS-Nozzle Case and for providing boundary conditions for the DNS. The RANS calculation simulates the full nozzle geometry that encompasses the DNS domain, including the converging and diverging nozzle sections that lead up to the test section. The flow is assumed to be fully turbulent throughout the nozzle; and the Reynolds stresses and turbulent heat flux are modeled via Menter's two equation, shear stress transport (SST) turbulence model. As seen in the top of Figure 1, the tunnel configuration starts with the converging section in advance of the nozzle throat, which is located at $x \approx 0$ m. The diverging section spans from $x \approx 0$ m to $x \approx 2.6$ m, followed by the test section region.

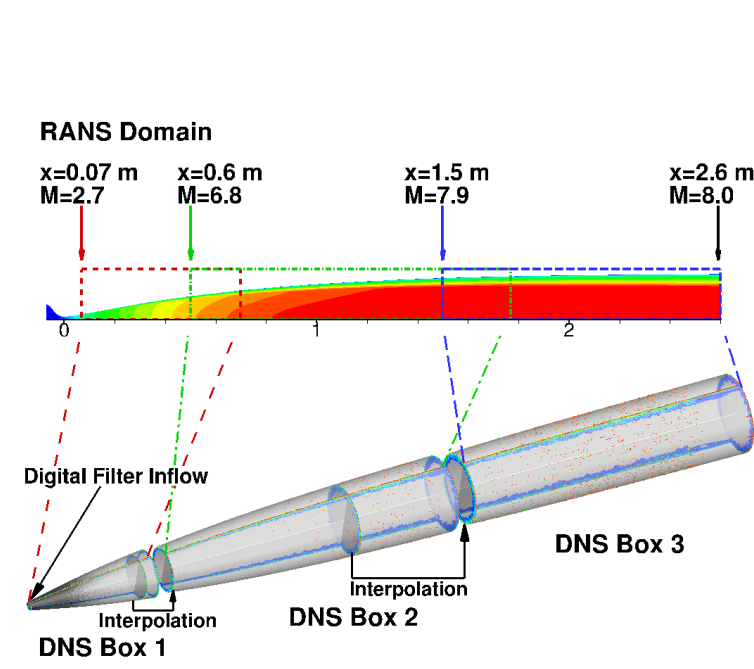


Fig. 1 Computational domain set up for (top) RANS, contours colored by Mach number, and (bottom) Case DNS-Nozzle, shown as numerical schlieren image with contours colored by the magnitude of vorticity to emphasize the large-scale motions within the boundary layer.

The expansion portion of the Laval nozzle is simulated using DNS. The DNS domain starts slightly downstream of the nozzle throat at $x = 0.07$ m with a local freestream Mach number of $M_\infty = 2.7$ and ends at the nozzle exit at $x = 2.6$ m with a freestream Mach number of $M_\infty \approx 8.0$. The DNSs are carried out in three stages involving overlapping streamwise domains as shown in Figure 1. The selected DNS domain covers the origin of most of the acoustic sources responsible for generating freestream noise in the test section because it includes the portion of the nozzle with high freestream Mach numbers and, thus, with large intensity of noise radiation. The combined streamwise length of the full simulation (Box-1 DNS + Box-2 DNS + Box-3 DNS) is $62.1 \delta_r$, where $\delta_r = 0.0407$ m is the boundary-layer thickness at $x = 2.336$ m where measurements of nozzle-wall pressure fluctuations are made (Section III.A). The streamwise domain length is long enough for the artificial inflow turbulence to develop based on our previous experience of DNS over a zero-pressure-gradient flat plate [18]. To prevent the reflection of any acoustic disturbances produced by the outflow boundary condition back into the flow regime of interest, an extra region was appended to the DNS domain of interest ($x \leq 2.6$ m). This appended region consists of an additional 30 streamwise grid points and the streamwise grid spacing is progressively stretched across the length of this region by using a stretching ratio of 1.1. Table 2 lays out the grid size and grid resolutions of the DNS mesh. A uniform grid distribution is used in the streamwise and azimuthal direction with grid spacings of $\Delta x^+ = 4.7$ and $\Delta y_{max}^+ = 8.0$, respectively, at the wall region of the measurement location ($x = 2.336$ m). Grid distribution in the radial direction is clustered near the nozzle wall with the near-wall grid spacing equal to $\Delta r^+ = 0.3$ at $x = 2.336$ m, and is kept uniform ($\Delta r^+ = 4.3$) in the free stream all the way to the nozzle axis. The above radial grid distribution ensures that both boundary layer and freestream regions are well resolved in the current DNS.

The non-uniform digital-filtering (DF) method [18, 19] is applied to generate inflow turbulence for Box 1 simulations. The mean boundary layer profiles and the Reynolds stress tensor at the inflow are extracted from Case RANS_HWT-8 at $x = 0.07$ m. The robustness and adequacy of the DF inflow method for predicting the global pressure field induced by hypersonic turbulent boundary layers has been demonstrated on both flat plate [18] and axisymmetric nozzle [14, 16] configurations. For Box 2 and Box 3 simulations, the inflow conditions are prescribed using saved flow data of the upstream DNS box. On the nozzle wall, no-slip conditions are applied for the three velocity components, and an isothermal condition is used for the temperature with $T_w = 298$ K. At the outflow boundary, unsteady nonreflecting boundary conditions based on Thompson [20] are imposed after introducing an outflow zone with a gradually stretched axial grid beyond the nozzle exit location. The polar-axis boundary condition mentioned above is used at the nozzle axis to remove the coordinate singularity in the axisymmetric grid. Finally, periodic boundary conditions are used in the azimuthal direction.

Table 2 Domain and mesh parameters for Case DNS-Nozzle. The boundary layer thickness δ_r and the viscous length $(z_\tau)_r$ are taken from those at $x = 2.336$ m. $\Delta y_{max} = R\Delta\theta$ is the linear azimuthal grid spacing at the wall.

Case	x_i (m)	x_e (m)	L_x (m)	N_x	N_θ	N_r	L_x/δ_r	Δx^+	Δy_{max}^+	Δr_{wall}^+	$\Delta r_{\infty,max}^+$
DNS Box 1	0.07	0.63	0.56	900	2048	238	13.8	9.4	4.6	0.2	40.4
DNS Box 2	0.6	1.87	1.27	2000	2048	731	31.2	9.4	7.2	0.3	4.0
DNS Box 3	1.5	2.6	1.1	3450	2048	731	27.0	4.7	8.0	0.3	4.3

III. DNS Validation

For the purpose of validating the aforementioned DNS methodology, the wind-tunnel facility and instrumentation for measuring turbulent wall pressure fluctuations are introduced. Additionally, an in-house hypersonic CFD code from Sandia National Laboratories is introduced, which is used to simulate a Mach 8 flat-plate turbulent boundary layer for cross-validating against Case DNS-FlatPlate.

A. Experiments of Turbulent Wall Pressure Fluctuations

Measurements of turbulent-boundary-layer wall pressure fluctuations were performed in the Sandia Hypersonic Wind Tunnel (HWT). The tunnel is a conventional blowdown-to-vacuum facility. Interchangeable nozzle and heater sections allow the tunnel to be run at Mach 5, 8 or 14. Run times were typically 30 s. Experiments are conducted only at Mach 8 for the present work. HWT-8 uses 689 MPa nitrogen supplied from a bottle farm. It has a P_0 range of 1720–6890 kPa, T_0 range of 500–890 K, and Re_{unit} can be varied from $3.3\text{--}20 \times 10^6/m$. Noise levels vary from 3–5% [21].

Turbulent boundary-layer pressure fluctuations on the nozzle wall were measured for varying freestream conditions. An array of both spanwise and axial sensors was used to attempt to capture the spatial correlation lengths in the turbulent boundary layer. The center of this array is located at an axial distance of $x = 2.336$ m from the nozzle throat. Figure 2 shows the layout of the sensors with respect to the flow and Table 3 lists the various sensor spacings.

Kulite Mic-062 transducers were used to measure nozzle wall pressure fluctuations between 0 and 50 kHz. They have a nominal resonant frequency of 125 kHz. The repeatability is approximately 0.1% of the full scale. The diameter of the sensors is 1.59 mm. The Kulites have screens to protect the diaphragms from damage. For these tests, A-screen sensors were used, which simply have a large central hole. This screen offers only a small amount of diaphragm protection, but the sensor has a flat frequency response up to 30–40% of the resonant frequency [22].

Higher frequency pressure fluctuations were studied with PCB132 sensors. The sensor is a very high frequency piezoelectric time-of-arrival sensor. The resonant frequency is above 1 MHz, and the flat portion of the response extends to at least several hundred kilohertz [22]. However, the internal PCB132 electronics effectively high-pass filter the data at 11 kHz, per the manufacturer’s specifications, so low frequency measurements cannot be made with these sensors.

An Endevo Model 136 DC Amplifier was used to apply a 10 V excitation to the Kulite sensors and supply a gain of 100 for signal output. A Krohn-Hite Model 3384 Tunable Active Filter provided an anti-aliasing low-pass Bessel filter. The filter was set at 200 kHz, had eight poles, and provided 48 dB attenuation per octave. The sampling frequency was 1 MHz for the Kulite sensor signals. The PCB132 sensor signals all ran through a PCB 482A22 signal conditioner that

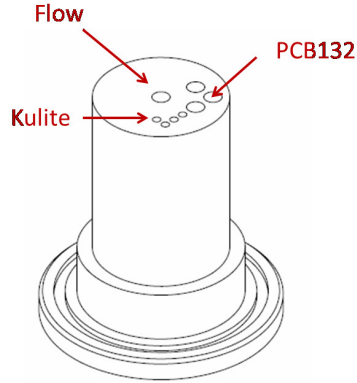


Fig. 2 Nozzle wall insert, located at $x = 2.336$ m from the throat.

Table 3 Pressure sensor locations with respect to center of the nozzle insert.

	x (mm)	y (mm)
PCB132 1 (P1)	0.00	0.00
PCB132 2 (P2)	7.62	-2.54
PCB132 3 (P3)	7.62	-7.62
PCB132 4 (P4)	2.54	-7.62
Kulite 1 (K1)	5.08	7.62
Kulite 2 (K2)	7.62	7.62
Kulite 3 (K3)	7.62	3.81
Kulite 4 (K4)	7.62	1.27

provided constant-current excitation to the built-in sensor amplifiers. It also decoupled the AC signal from the DC bias voltage. The output from the signal conditioner was fed through a Krohn-Hite Model 3944 Filter with a 1 MHz low-pass anti-aliasing Bessel filter. This filter had four poles and offered 24 dB of attenuation per octave. The sampling frequency for the PCB132 sensor signals was 2.5 MHz. Data were acquired using a National Instruments PXI-1042 chassis with 14-bit PXI-6133 modules (10 MHz bandwidth).

The measurements of wall-pressure fluctuations by Kulite and PCB132 sensors are compared to the predictions by the DNS (Case DNS-Nozzle) in Section IV.

B. DNS with SPARC CFD code

In conjunction with the simulations described in Section II, DNS of Mach 8 turbulent flow over a flat plate is conducted using the Sandia Parallel Aerodynamics Research Code (SPARC), which is a shock-capturing CFD code under development at Sandia National Laboratories. This code is designed to run on next-generation computing architectures and scale efficiently on exascale-class computing platforms. SPARC supports a variety of numerical schemes for hypersonic flow simulation, but in this work it operates as a cell-centered finite volume code. In order to conduct compressible turbulence simulations, the code uses the kinetic energy consistent finite volume scheme developed by Subbareddy and Candler [23]. This scheme is implemented with fourth order spatial accuracy, produces discrete fluxes of kinetic energy that are consistent with the fluxes of the discrete momentum and continuity equations, and requires no explicit dissipation for stabilization in smooth flowfields. As described by Subbareddy and Candler[23], the scheme switches on additional dissipative terms from the modified Steger-Warming scheme [24] in regions near shock waves, thus providing stabilization in the presence of sharp gradients, but excludes these stabilization terms in smooth regions of the flow. In this work, a switch based on the Mach number [25] is used to detect shocks and activate these stabilizing terms. The result is that the overall scheme is stable in the presence of shock waves, yet delivers high accuracy and low numerical dissipation in smooth regions, such as turbulent boundary layers. This technique is of course only applicable

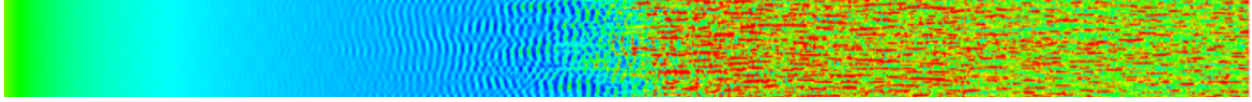


Fig. 3 Instantaneous snapshot of wall shear stress for Mach 8 flow over a flat plate. Flow is perturbed with acoustic waves in the freestream to trigger transition to turbulence.

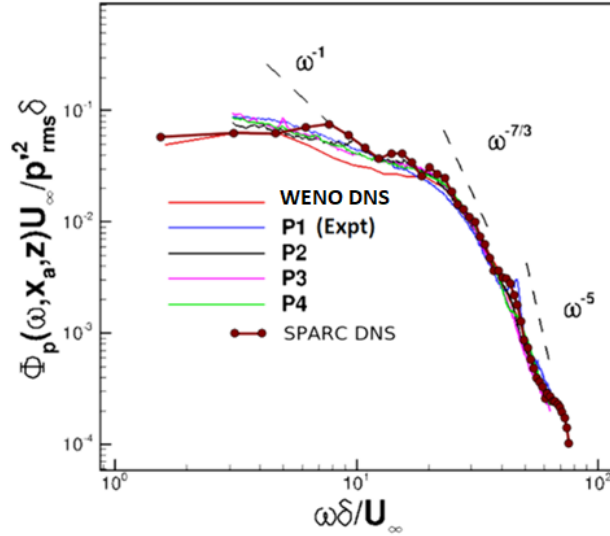


Fig. 4 Comparison of dimensionless power spectrum from experiments and DNS for Mach 8 flow over a flat plate. The lines P1-P4 correspond to measurements from pressure transducers in the Sandia HWT-8 wind tunnel. The line “WENO DNS” represents the DNS method described in Section II with $Re/m = 8.2 \times 10^6$ and $Re_\tau = 386$, while the line “SPARC DNS” corresponds to DNS using the SPARC code as described in Section III.B with $Re/m = 42 \times 10^6$ and $Re_\tau = 353$.

when the turbulence Mach number is low and eddy shocklets are absent, which is the case here.

The turbulent DNS carried out using the SPARC code mirrors the “DNS-FlatPlate” case described in Section II and uses the flow conditions given in Table 1. However, rather than using the recycling plane technique, a fully transitional boundary layer for flow over a flat plate is simulated. The laminar flow established at the leading edge of the plate is perturbed with acoustic waves originating in the freestream, which have a frequency and wavelength close to those of the most unstable waves of the second mode instability. These perturbations then excite second mode instability waves, which amplify and rapidly break down into fully-developed turbulence. An example of the resulting instantaneous wall shear stress pattern is given in Fig. 3, illustrating the growth of instability waves and the subsequent transitional and turbulent flow. Figure 4 compares power spectra of the wall pressure from experimental measurements in the Sandia HWT-8 wind tunnel with those predicted by DNS codes. For DNS with the SPARC code, the power spectra are taken from the fully turbulent region near the downstream end of the plate. Good agreement between both DNS codes and the measurements is observed.

IV. Results

In this section, DNS results for the nozzle-wall turbulent boundary layer (Case DNS-Nozzle) are presented. The mean and turbulence statistics within the boundary layer are compared with those of RANS. Moreover, the single- and multi-point statistics of wall pressure fluctuations induced by the nozzle-wall turbulent boundary layer are analyzed and compared with the experiments as discussed in Section III.A. For Case DNS-Nozzle, averages are first calculated over azimuthal locations for each instantaneous flow field; then, an ensemble average over 78 flow-field snapshots spanning a time interval of 0.924 ms (corresponding to approximately $27\delta_r/U_\infty$) is calculated. To monitor the statistical convergence, flow statistics are computed by averaging over the whole or half the number of the flow-field snapshots, and a negligible difference ($<1\%$) is observed between the two. Power spectra are calculated using the Welch method [26]

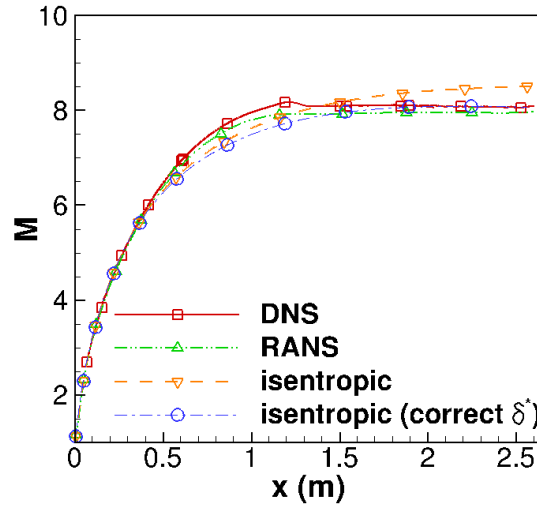


Fig. 5 Mach number distribution along the nozzle axis.

with one segment. A Hamming window is used for weighting the data prior to the fast Fourier transform (FFT) processing. The sampling frequency is 8.33 MHz (corresponding to approximately $27\delta_r/U_\infty$), and the length of an individual segment is 0.924 ms (approximately $27\delta_r/U_\infty$).

Table 4 lists the properties of nozzle-wall turbulent boundary layer at the measurement location ($x = 2.336$ m). Three sets of results are included in the table, based on the RANS calculations (Case RANS-Nozzle), the DNS (Case DNS-Nozzle), and the empirical estimates derived from the Pate correlation [27]. The latter correlation allows one to deduce the boundary layer displacement thickness, δ^* , and the nozzle wall friction coefficient, C_f . The shape factor H , boundary-layer thickness, and the momentum thickness of the tunnel-wall boundary layer, as well as the Reynolds numbers based on these parameters, are then estimated using an empirical relation by Wood [28] and a power law profile with an exponent of 1/9 [29]. Overall, favorable comparisons in boundary-layer parameters are found among DNS, RANS and the empirical relations.

Table 4 Boundary layer properties at $x = 2.336$ m.

Case	M_∞	T_w (K)	Re_{unit} (1/m)	Re_θ	Re_τ	Re_{δ_2}	δ (mm)	δ^* (mm)	θ (mm)	z_τ (μ m)	C_f (10^{-4})	u_τ (m/s)
Pate	7.91	298	12.3×10^6	9249	648	1607	37.6	23.7	0.76	58.0	8.9	60.1
RANS	7.80	298	12.7×10^6	22075	671	3971	44.7	25.1	1.74	67.0	6.1	47.4
DNS	8.06	298	12.3×10^6	17253	580	3045	40.7	18.8	1.50	69.0	6.2	49.7

Figure 5 shows the Mach number distribution along the nozzle axis. Good comparison is achieved for the freestream Mach number distribution among DNS, RANS, and the inviscid isentropic theory that is corrected by local displacement thickness. Figures 6 and 7 show the radial distribution of the mean boundary-layer profiles and the Reynolds shear stress, respectively, at the measurement location ($x = 2.336$ m) and the nozzle exit ($x = 2.6$ m). For the RANS case, the Reynolds shear stress is calculated by using the Boussinesq approximation. The predictions for the mean properties and Reynolds shear stress match rather well between the DNS and the RANS results. Considering that the DNS domain, which consists of a section of the nozzle, is embedded within the RANS domain with the full-tunnel geometry, the favorable match between DNS and RANS results confirms that the tunnel nozzle flow is adequately reproduced with the DNS subdomain by using the inflow boundary conditions provided by the RANS.

Figure 8 shows the rms of wall-pressure fluctuations as a function of axial locations. In the same figure, the rms pressure fluctuations measured by PCB transducers are reported as well. Good comparisons in fluctuating pressure intensities between DNS and PCB transducers are achieved. The comparisons in fluctuating pressure intensities between DNS and Kulite transducers are not included, given that the pressure signals of the DNS have not been collected for a

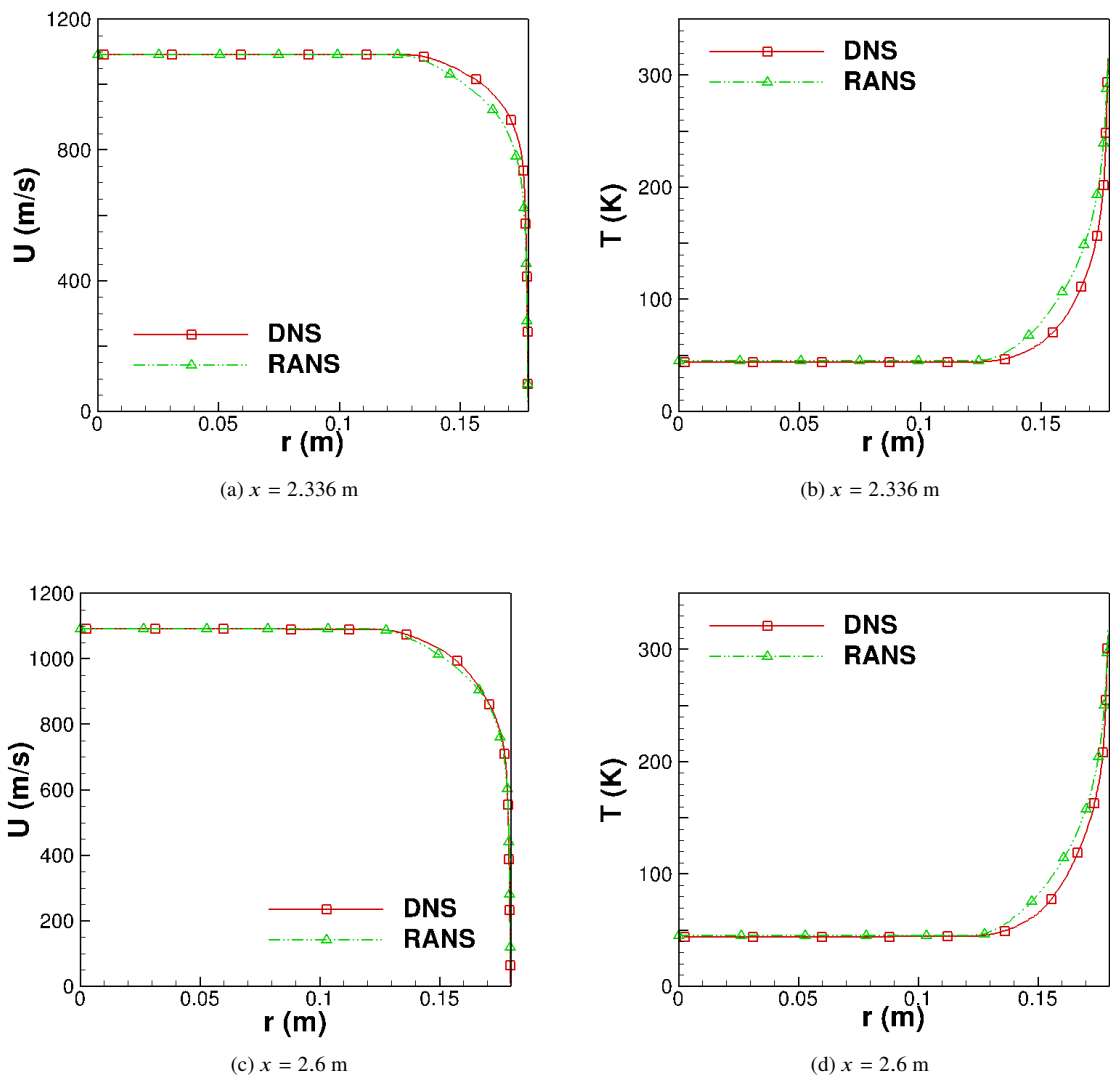


Fig. 6 Radial distribution of the streamwise velocity at axial locations of $x = 2.336$ m and $x = 2.6$ m.

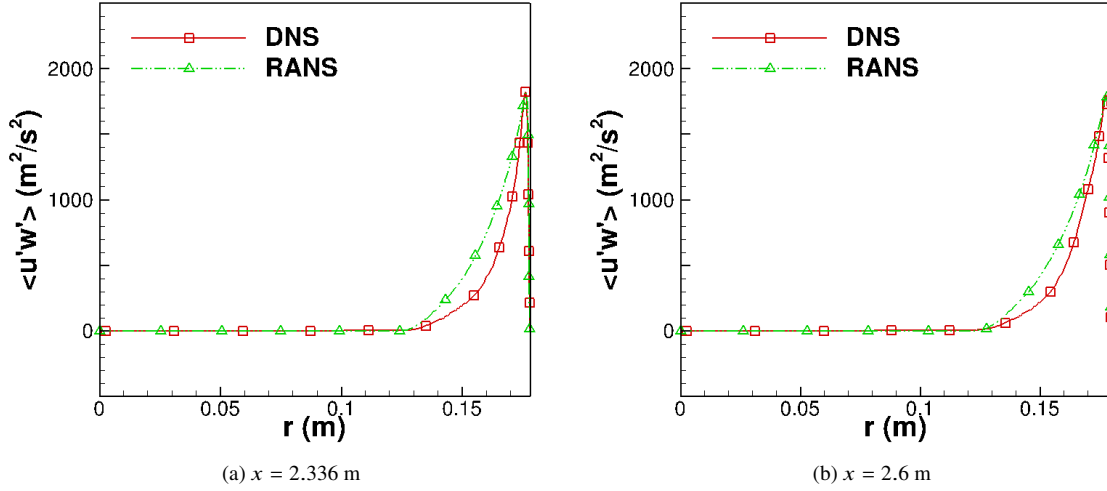


Fig. 7 Radial distribution of the Reynolds shear stress at axial locations of $x = 2.336$ m and $x = 2.6$ m.

long enough time period to cover a frequency bandwidth comparable to that of Kulite sensors.

Figure 9 shows a comparison in power spectral density (PSD) of surface pressure fluctuations between numerical predictions and wind-tunnel measurements. Very good agreement of wall-pressure PSD between the DNS and the experiments has been achieved at high frequencies. These high frequencies are especially relevant to the excitation of second mode (i.e., Mack mode) instabilities of boundary layer flows over test articles in hypersonic wind tunnels.

In addition to the intensity and PSD of the pressure fluctuations, the coherence function represents another basic ingredient for developing statistical pressure fluctuation models. The coherence function is defined as

$$\Gamma^2(\Delta x, \Delta y, \omega) = \frac{|\Phi_{P_a P_b}(\Delta x, \Delta y, \omega)|^2}{|\Phi_{P_a P_a}(\omega)| |\Phi_{P_b P_b}(\omega)|} \quad (1)$$

where $\Phi_{P_a P_b}(\Delta x, \Delta y, \omega) = \overline{\tilde{p}^*(x, y, \omega) \tilde{p}(x + \Delta x, y + \Delta y, \omega)}$ is the cross-power spectral density between two arbitrary points a and b separated by the distance Δx , Δy in streamwise and spanwise directions, respectively, with \tilde{p} the time-Fourier transform of the pressure fluctuations. $\Phi_{P_a P_a}(\omega)$ and $\Phi_{P_b P_b}(\omega)$ are the pressure auto-spectra at a and b , respectively.

Figure 10 plots a comparison in coherence of wall pressure fluctuations between numerical predictions and the measurements by PCB132 sensors. Good comparisons in coherence are achieved for the two transducers P2 and P3 that have a spanwise separation only as well as for the two transducers P2 and P4 that have both nonzero streamwise and spanwise separations. A significant mismatch between DNS and experiments is shown for the two transducers P3 and P4 that are aligned in the direction of the airstream with a zero spanwise separation. The mismatch could be caused by the installation flushness of pressure transducers [30] or the surface discontinuity of installing a flat sensor in a contoured surface. However, further research is necessary to identify the exact cause of the mismatch.

The effect of the separation distance on the streamwise and spanwise coherence of wall pressure obtained by the computational data is presented in Figure 11 in terms of the non-dimensional frequency $\omega \Delta x / U_c$ and $\omega \Delta y / U_c$, respectively. In the same figure, the Corcos analytical approximation [31] is reported as well. According to Corcos, the coherence function is modeled as

$$\Gamma_{ab}(\Delta x, \Delta y, \omega) = e^{-\alpha_1 \omega |\Delta x| / U_c} e^{-\alpha_2 \omega |\Delta y| / U_c} e^{i \omega \Delta x / U_c} \quad (2)$$

where the parameters α_1 and α_2 quantify the loss of coherence along the longitudinal and transverse directions, respectively. These parameters are selected by suitable fit of DNS data. The Corcos model delivers good prediction of wall pressure coherence over intermediate and high frequencies but fails in the low-frequency range. A similar trend has been reported by Di Marco et al. [32] for flat-plate turbulent boundary layers at Mach 2 to 4. The streamwise and

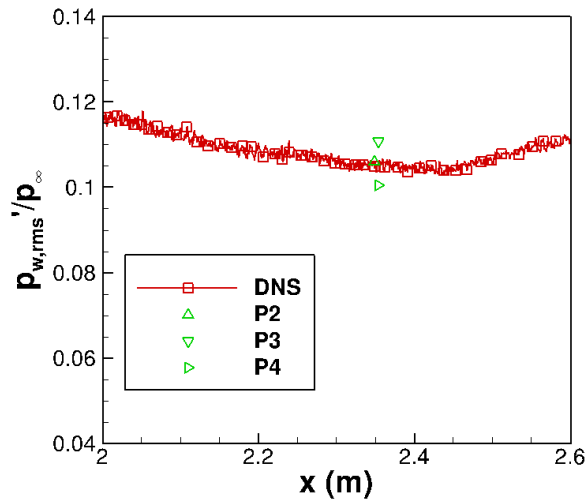


Fig. 8 Comparison in rms of surface pressure fluctuations between numerical predictions (Case DNS-Nozzle) and wind-tunnel measurements.

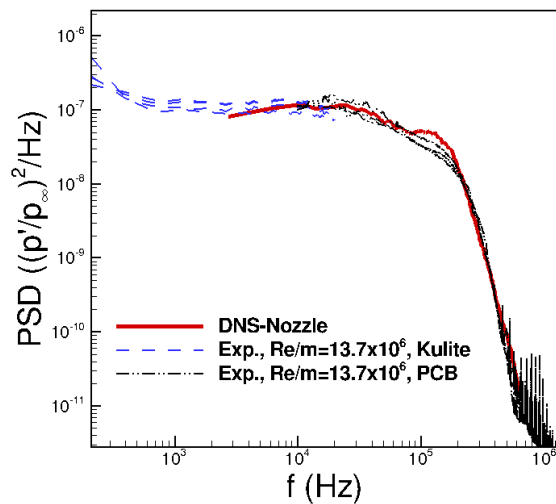


Fig. 9 Comparison in power spectral density of surface pressure fluctuations between numerical predictions (Case DNS-Nozzle) and wind-tunnel measurements.

spanwise decay constants at Mach 8 are similar to those predicted by DNS at lower supersonic Mach numbers [32] and those identified from the wind tunnel experiments by Beresh et al. [33] at Mach 2 [34].

V. Summary

This paper has outlined preliminary findings from ongoing direct numerical simulations of the nozzle-wall turbulent boundary layer inside a Mach 8 hypersonic wind tunnel and the comparison of the DNS with experimental measurements at the same tunnel. The axisymmetric nozzle geometry and the flow conditions of the DNS match those of the Sandia Hypersonic Wind Tunnel at Mach 8. The mean and turbulence statistics of the nozzle-wall turbulent boundary layer predicted by DNS compare well with those of Pate's correlation and the larger domain RANS simulation. The DNS-predicted wall-pressure intensity and PSD show good comparisons with those measured by surface-mounted PCB132 sensors. Comparisons with experiments in wall-pressure coherence are also conducted for the first time at such a high Mach number. The wall-pressure coherence predicted by DNS shows good comparisons with that measured by two PCB transducers with nonzero spanwise separations. The comparison is less favorable, however, for coherence that is measured by two PCB sensors that are streamwise aligned (i.e., with zero spanwise separation). Consistent with previous studies at lower Mach numbers, the Corcos model is shown to deliver good prediction of wall pressure coherence over intermediate and high frequencies but to fail in the low-frequency range. The streamwise and spanwise decay constants at Mach 8 are similar to those predicted by DNS and experiments at lower supersonic Mach numbers.

Future work will include DNS computations of pressure fluctuations over a cone model under the noisy flow in Sandia HWT-8 for direct comparisons to the cone surface measurements and a comparison of DNS-predicted pressure fluctuations over the nozzle wall with those over the cone surface.

Acknowledgments

Financial support for the work is being provided by the Sandia National Laboratories under subcontract number PO-1885712. Partial support was also provided by the Office of Naval Research (under grant N00014-17-1-2347). Computational resources were provided by the DoD High Performance Computing Modernization Program and the NSF PRAC program (NSF ACI-1640865). Sandia National Laboratories is a multimission laboratory managed and operated by National Technology and Engineering Solutions of Sandia, LLC., a wholly owned subsidiary of Honeywell International, Inc., for the U.S. Department of Energy's National Nuclear Security Administration under contract DE-NA0003525. The views and conclusions contained herein are those of the authors and should not be interpreted as necessarily representing the official policies or endorsements, either expressed or implied, of the funding agencies or the U.S. Government.

References

- [1] Casper, K. M., Beresh, S. J., Henfling, J. F., Spillers, R. W., and Pruett, B. O. M., "Hypersonic Wind-Tunnel Measurements of Boundary-Layer Transition on a Slender Cone," *AIAA Journal*, Vol. 54, No. 4, 2016, pp. 1250–1263.
- [2] Smith, J. A., DeChant, L. J., Casper, K. M., Mesh, M., and R. V. Field, J., "Comparison of a Turbulent Boundary Layer Pressure Fluctuation Model to Hypersonic Cone Measurements," AIAA Paper 2016-4047, 2016.
- [3] Schneider, S. P., "Developing Mechanism-based Methods for Estimating Hypersonic Boundary-Layer Transition in Flight: The Role of Quiet Tunnels," *Progress in Aerospace Sciences*, Vol. 72, 2015, pp. 17–29.
- [4] Keyes, F. G., "A Summary of Viscosity and Heat-Conduction Data for He, A, H_2 , O_2 , CO , CO_2 , H_2O , and Air," *Transactions of the American Society of Mechanical Engineers*, Vol. 73, 1951, pp. 589–596.
- [5] Jiang, G. S., and Shu, C. W., "Efficient Implementation of Weighted ENO Schemes," *Journal of Computational Physics*, Vol. 126, No. 1, 1996, pp. 202–228.
- [6] Taylor, E. M., Wu, M., and Martín, M. P., "Optimization of Nonlinear Error Sources for Weighted Non-Oscillatory Methods in Direct Numerical Simulations of Compressible Turbulence," *Journal of Computational Physics*, Vol. 223, No. 1, 2006, pp. 384–397.
- [7] Wu, M., and Martín, M. P., "Direct Numerical Simulation of Supersonic Boundary Layer over a Compression Ramp," *AIAA Journal*, Vol. 45, No. 4, 2007, pp. 879–889.
- [8] Williamson, J., "Low-Storage Runge-Kutta Schemes," *Journal of Computational Physics*, Vol. 35, No. 1, 1980, pp. 48–56.

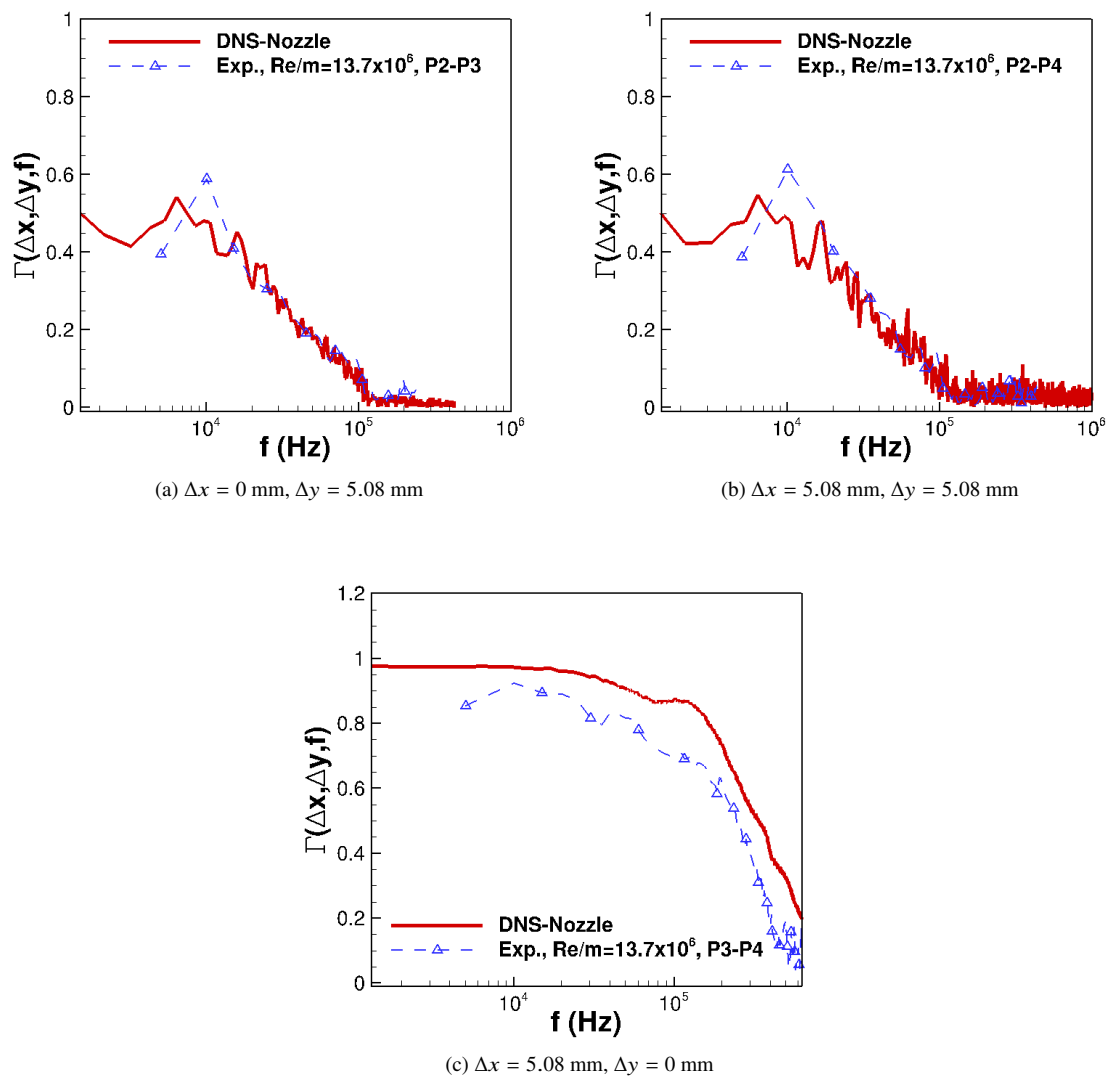


Fig. 10 Comparison in coherence of surface pressure fluctuations between numerical predictions (Case DNS-Nozzle) and wind-tunnel measurements.

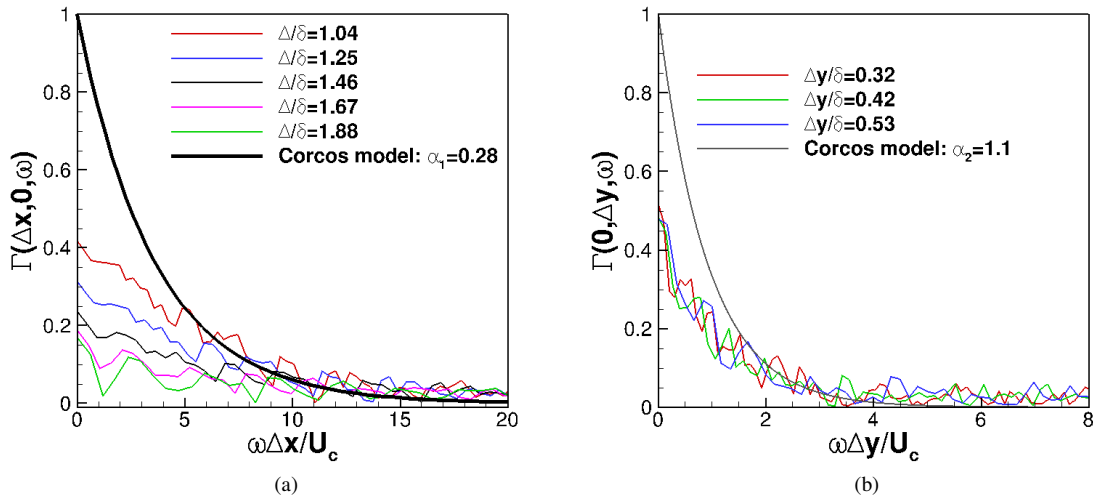


Fig. 11 Streamwise and spanwise coherence as a function of the normalized frequency at $x = 2.336$ m for Case DNS-Nozzle. The solid line represent the Corcos model with exponents of $\alpha_1 = 0.28$ and $\alpha_2 = 1.1$.

- [9] Mohseni, K., and Colonius, T., “Numerical Treatment of Polar Coordinate Singularities,” *Journal of Computational Physics*, Vol. 157, 2000, pp. 787–795.
- [10] Constantinescu, G. S., and Lele, S. K., “A Highly Accurate Technique for the Treatment of Flow Equations at the Polar Axis in Cylindrical Coordinates Using Series Expansions,” *Journal of Computational Physics*, Vol. 183, 2002, pp. 165–186.
- [11] Bogey, C., de Cacqueray, N., and Bailly, C., “Finite Differences for Coarse Azimuthal Discretization and for Reduction of Effective Resolution Near Origin of Cylindrical Flow Equations,” *Journal of Computational Physics*, Vol. 230, 2011, pp. 1134–1146.
- [12] Duan, L., Choudhari, M. M., and Wu, M., “Numerical Study of Pressure Fluctuations due to a Supersonic Turbulent Boundary Layer,” *Journal of Fluid Mechanics*, Vol. 746, 2014, pp. 165–192.
- [13] Duan, L., Choudhari, M. M., and Zhang, C., “Pressure Fluctuations Induced by a Hypersonic Turbulent Boundary Layer,” *Journal of Fluid Mechanics*, Vol. 804, 2016, pp. 578–607.
- [14] Huang, J., Zhang, C., Duan, L., and Choudhari, M. M., “Direct Numerical Simulation of Hypersonic Turbulent Boundary Layers inside an Axisymmetric Nozzle,” AIAA Paper 2017-0067, 2017.
- [15] Huang, J., L. Duan, L., and Choudhari, M. M., “Direct Numerical Simulation of Acoustic Noise Generation from the Nozzle Wall of a Hypersonic Wind Tunnel,” AIAA Paper 2017-3631, 2017.
- [16] Duan, L., Choudhari, M. M., Chou, A., Munoz, F., Ali, S. R. C., Radespiel, R., Schilden, T., Schröder, W., Marineau, E. C., Casper, K. M., Chaudhry, R. S., Candler, G. V., Gray, K. A., Sweeney, C. J., and Schneider, S. P., “Characterization of Freestream Disturbances in Conventional Hypersonic Wind Tunnels,” AIAA Paper 2018-0347, 2018.
- [17] “ANSYS Fluent User Guide, Release 16.1,” ANSYS Inc., 2016.
- [18] Huang, J., Zhang, C., and Duan, L., “Turbulent Inflow Generation for Direct Simulations of Hypersonic Turbulent Boundary Layers and their Freestream Acoustic Radiation,” *46th AIAA Fluid Dynamics Conference*, 2016, p. 3639.
- [19] Dhamankar, N. S., Martha, C. S., Situ, Y., Aikens, K. M., Blaisdell, G. A., and Lyrintzis, A. S., “Digital Filter-Based Turbulent Inflow Generation for Jet Aeroacoustics on Non-Uniform Structured Grids,” AIAA Paper 2014-1401, 2014.
- [20] Thompson, K. W., “Time Dependent Boundary Conditions for Hyperbolic Systems,” *Journal of Computational Physics*, Vol. 68, No. 1, 1987, pp. 1–24.

- [21] Casper, K. M., Beresh, S. J., Henfling, J. F., Spillers, R. W., Pruett, B. O. M., and Schneider, S. P., "Hypersonic Wind-Tunnel Measurements of Boundary-Layer Pressure Fluctuations," AIAA Paper 2009-4054, 2009.
- [22] Beresh, S. J., Henfling, J. F., Spillers, R. W., and Pruett, B. O. M., "Fluctuating Wall Pressures Measured beneath a Supersonic Turbulent Boundary Layer," *Physics of Fluids*, Vol. 23, No. 7, 2011.
- [23] Subbareddy, P. K., and Candler, G. V., "A fully discrete, kinetic energy consistent finite-volume scheme for compressible flows," *Journal of Computational Physics*, Vol. 228, 2009, pp. 1347–1364.
- [24] MacCormack, R., and Candler, G. V., "The solution of the Navier-Stokes equations using Gauss-Seidel line relaxation," *Computers and Fluids*, Vol. 17, No. 1, 1989, pp. 135–150.
- [25] Jaisankar, S., and Rao, S. V. R., "Diffusion regulation for Euler solvers," *Journal of Computational Physics*, Vol. 221, 2007, pp. 577–599.
- [26] Welch, P. D., "The Use of Fast Fourier Transform for the Estimation of Power Spectra: A Method Based on Time Averaging Over Short, Modified Periodograms," *IEEE Trans. Audio Electroacoustics*, Vol. AU-15, 1967, pp. 70–73.
- [27] Pate, S. R., "Dominance of Radiated Aerodynamic Noise on Boundary-Layer Transition in Supersonic-Hypersonic Wind Tunnels," Tech. rep., AEDC-TR-77-107, Arnold Engineering Development Center, 1978.
- [28] Wood, N., "Calculation of the Turbulent Boundary Layer in the Nozzle of an Intermittent Axisymmetric Hypersonic Wind Tunnel," *Aeronautical Research Council C.P. No. 721*, 1963.
- [29] Smits, A. J., and Dussauge, J. P., *Turbulent Shear Layers in Supersonic Flow*, 2nd ed., American Institute of Physics, 2006.
- [30] Hanly, R. D., "Effects of Transducer Flushness on Fluctuating Surface Pressure Measurements," AIAA Paper 1975-0534, 1975.
- [31] Corcos, G. M., "The Structure of the Turbulent Pressure Field in Boundary-Layer Flows," *Journal of Fluid Mechanics*, Vol. 18, 1964, pp. 353–378.
- [32] Di Marco, A., Camussi, R., Bernardini, M., and Pirozzoli, S., "Wall Pressure Coherence in Supersonic Turbulent Boundary Layers," *Journal of Fluid Mechanics*, Vol. 732, 2013, pp. 445–456.
- [33] Beresh, S. J., Henfling, J. F., Spillers, R. W., and Pruett, B. O. M., "Very-Large-Scale Coherent Structures in the Wall Pressure Field Beneath a Supersonic Turbulent Boundary Layer," *Physics of Fluids*, Vol. 25, No. 9, 2013.
- [34] DeChant, L. J., and Smith, J. A., "Band Limited Correlation Estimates for $A(\xi\omega/U)$ and $B(\eta\omega/U)$ Using Beresh et. al. 2013 Data Sets," Tech. rep., SAND2014-1123, 2014.